



## Cryo-EM structure of respiratory complex I reveals a link to mitochondrial sulfur metabolism

Edoardo D'Imprima<sup>a</sup>, Deryck J. Mills<sup>a</sup>, Kristian Parey<sup>a</sup>, Ulrich Brandt<sup>b,c</sup>, Werner Kühlbrandt<sup>a</sup>, Volker Zickermann<sup>c,d,\*</sup>, Janet Vonck<sup>a,\*\*</sup>

<sup>a</sup> Max Planck Institute of Biophysics, Department of Structural Biology, Max-von-Laue-Str. 3, 60438 Frankfurt am Main, Germany

<sup>b</sup> Radboud Center for Mitochondrial Medicine, Radboud University Medical Center, 6525 GA Nijmegen, The Netherlands

<sup>c</sup> Cluster of Excellence Frankfurt "Macromolecular Complexes," Goethe University, 60438 Frankfurt am Main, Germany

<sup>d</sup> Structural Bioenergetics Group, Institute of Biochemistry II, Medical School, Goethe University Frankfurt, Max-von-Laue-Str. 9, 60438 Frankfurt am Main, Germany

### ARTICLE INFO

#### Article history:

Received 20 July 2016

Received in revised form 22 September 2016

Accepted 29 September 2016

Available online 30 September 2016

#### Keywords:

Complex I

NADH:ubiquinone oxidoreductase

Electron transport chain

Sulfur metabolism

Mitochondria

Cryo-electron microscopy

### ABSTRACT

Mitochondrial complex I is a 1 MDa membrane protein complex with a central role in aerobic energy metabolism. The bioenergetic core functions are executed by 14 central subunits that are conserved from bacteria to man. Despite recent progress in structure determination, our understanding of the function of the ~30 accessory subunits associated with the mitochondrial complex is still limited. We have investigated the structure of complex I from the aerobic yeast *Yarrowia lipolytica* by cryo-electron microscopy. Our density map at 7.9 Å resolution closely matches the 3.6–3.9 Å X-ray structure of the *Yarrowia lipolytica* complex. However, the cryo-EM map indicated an additional subunit on the side of the matrix arm above the membrane surface, pointing away from the membrane arm. The density, which is not present in any previously described complex I structure and occurs in about 20% of the particles, was identified as the accessory sulfur transferase subunit ST1. The *Yarrowia lipolytica* complex I preparation is active in generating H<sub>2</sub>S from the cysteine derivative 3-mercaptopyruvate, catalyzed by ST1. We thus provide evidence for a link between respiratory complex I and mitochondrial sulfur metabolism.

© 2016 The Authors. Published by Elsevier B.V. This is an open access article under the CC BY-NC-ND license (<http://creativecommons.org/licenses/by-nc-nd/4.0/>).

### 1. Introduction

Mitochondrial NADH:ubiquinone oxidoreductase (respiratory complex I) is a 1 MDa multi-subunit membrane protein complex that has a central role as a proton pump in eukaryotic energy conversion [1,2]. Complex I couples electron transfer from NADH to ubiquinone to translocation of protons across the inner mitochondrial membrane, generating about 40% of the proton motive force that drives ATP synthesis. Complex I has been shown to release toxic oxygen radicals that contribute e.g. to tissue damage in myocardial infarction [3]. Complex I dysfunction is a common cause of mitochondrial disorders and has been implicated in the pathogenesis of neurodegenerative diseases [4,5]. Fourteen central

subunits that are conserved from bacteria to man form the catalytic core of complex I. The core subunits, which are sufficient for function, are assigned to three functional modules: the N module for NADH oxidation, the Q module for ubiquinone reduction and the P module for proton pumping [2,6]. The precise roles of the ~30 accessory subunits of eukaryotic complex I are not yet thoroughly characterized [7].

The structure of the core subunits has been determined by X-ray crystallography of bacterial complex I [8–10]. The structure of the mammalian complex was determined by cryo-EM at 5 Å resolution [11] and more recently at 4.2 and 3.9 Å [12,13], and an intermediate-resolution X-ray structure of a bovine complex I fragment has been reported [14]. Together, these structures provide the topology of all mammalian accessory subunits. The 3.6–3.9 Å X-ray structure of mitochondrial complex I from the aerobic yeast *Yarrowia lipolytica* [15] provided insights into the mechanism of redox-linked proton translocation and a regulatory switch between active and inactive forms of the enzyme. However, detailed information on the structure and function of accessory complex I subunits is still limited.

The family of sulfur transferases (E.C. 2.8.1) comprises a group of proteins that catalyze the formation and interconversion of compounds containing sulfane sulfur atoms [16]. Sulfur transferases are present in organisms of all phyla. Although these proteins differ significantly at

**Abbreviations:** 2D, two-dimensional; 3D, three-dimensional; cryo-EM, cryo-electron microscopy; CTF, contrast transfer function; FSC, Fourier Shell Correlation; MST, 3-mercaptopyruvate:sulfur transferase; MTF, modulation transfer function; SQR, sulfide quinone reductase; TMH, transmembrane helix; TST, thiosulfate:sulfur transferase.

\* Correspondence to: V. Zickermann, Structural Bioenergetics Group, Institute of Biochemistry II, Medical School, Goethe University Frankfurt, Max-von-Laue-Str. 9, 60438 Frankfurt am Main, Germany.

\*\* Corresponding author.

E-mail addresses: [zickermann@med.uni-frankfurt.de](mailto:zickermann@med.uni-frankfurt.de) (V. Zickermann), [janet.vonck@biophys.mpg.de](mailto:janet.vonck@biophys.mpg.de) (J. Vonck).

the sequence level, the tandem domain three-dimensional structure seems to be highly conserved and resembles that of bovine rhodanese, the most studied and best characterized sulfur transferase [17].

Abdrakhmanova et al. [18] showed that a sulfur transferase is associated with *Y. lipolytica* complex I. The recent development of direct electron detectors, improvements in image processing software algorithms and faster computers have made it possible to produce high-resolution maps by cryo-EM [19,20] and to separate particles with different conformations or subunit composition in the same dataset [21, 22]. We here report the cryo-EM structure of *Y. lipolytica* complex I. Roughly 20% of the complexes contributing to the map had an additional density on the matrix arm, which was identified as the accessory complex I sulfur transferase subunit ST1. We discuss implications for a link between complex I and mitochondrial sulfur metabolism.

## 2. Materials & Methods

### 2.1. Protein purification and functional characterization

Complex I was purified in dodecyl-maltoside by His-tag affinity and size exclusion chromatography [23]. MST activity of complex I was measured using the lead sulfide assay [24,25]. Briefly, the assay mixture containing 100 mM HEPES buffer pH 7.4, 0.4 mM PbNO<sub>3</sub>, 100 µg/ml BSA, 30 mM DTT and varying amounts of 3-mercaptopyruvate was incubated at 37 °C for 4 min. The reaction was started by addition of the protein sample and formation of PbS was monitored at 390 nm with a Shimadzu UV-2450 spectrophotometer.

### 2.2. Cloning, protein expression and purification of recombinant ST1

The codon-optimized *st1* gene from *Y. lipolytica* was cloned into the expression vector pET-26b (Novagen, Germany) harboring a C-terminal His<sub>6</sub>-tag. The recombinant protein was overexpressed in *E. coli* BL21(DE3) pLysS cells (Novagen, Darmstadt) using liquid broth medium at 37 °C and 150 rpm agitation. Expression of ST1 was induced at OD<sub>600</sub> of 0.5–0.6 by adding IPTG to a final concentration of 1 mM. Cells were harvested, resuspended in 50 mM K-phosphate pH 7.5, 200 mM NaCl and broken by several passages through a cell disruptor (model TS, I&L Biosystems, Germany). Insoluble components were removed by centrifugation at 50,000 × g at 4 °C. The supernatant was loaded onto a HisTrap HP column (GE Healthcare; USA) and eluted with a step gradient of 20 mM, 40 mM and 250 mM imidazole. The protein was concentrated by ultrafiltration (Amicon Ultra-4, 10 kDa cutoff; Millipore, Germany) and loaded onto a Superdex 75 10/300 GL gel filtration column (GE Healthcare) equilibrated with 30 mM Tris-HCl pH 7.5, 100 mM NaCl and 5% glycerol. Protein was concentrated to 10 mg/ml and stored at 100 K.

### 2.3. Cryo-EM data collection

3 µl of a complex I sample at a concentration of 3 mg/ml was applied to freshly glow discharged Quantifoil R2/2 holey carbon grids (Quantifoil Micro Tools, Germany) that had been pretreated in chloroform for 1–2 h. The grids were blotted for 8–10 s at 70% humidity and 10 °C in an FEI Vitrobot plunge-freezer. Cryo-EM images were collected on a FEI Tecnai Polara operating at 300 kV carefully aligned as previously described [26] equipped with a Falcon II direct detector operating in movie mode. Images were recorded manually at a nominal magnification of 59,000× yielding a pixel size at the specimen of 1.77 Å. The camera system recorded 17 frames/s as described [27]. Videos were collected for 1.5 s with a total of 24 frames with a calibrated dose of about 3.5 e<sup>-</sup>/Å<sup>2</sup> per frame, at defocus values between –1.3 and –4.5 µm.

### 2.4. Image processing

A set of 2250 micrographs was collected. Whole-image drift correction of each movie was performed using the algorithm developed by [28]. Particles were picked using the semi-automatic procedure of EMAN Boxer [29], and the micrograph-based CTF was determined using CTFFIND3 [30] in the RELION workflow [31]. Where necessary, the contrast transfer function (CTF) was double-checked using the particle-based CTF procedure in EMAN2 [32]. The initial dataset contained 50,314 particle images (224 × 224 pixels) from 2184 selected micrographs. The particles were subjected to two-dimensional reference-free and three-dimensional (2D, 3D) classification in RELION [31] to discard imperfect particles. Visual selection of particle classes with interpretable features resulted in a dataset of 44,936 particle images for the first 3D consensus refinement. A map based on the low-resolution X-ray structure of *Y. lipolytica* complex I [6] was low-pass filtered to 60 Å and used as an initial model for the 3D refinement in RELION. Whole-image drift correction [28] over all the frames was followed by statistical movie processing, using running averages of seven movie frames and a standard deviation of one pixel for the translational alignment. Subsequently the particle polishing procedure implemented in RELION 1.3 was used to account for individual beam-induced particle translations and to calculate a frequency-dependent weight for the contribution of individual movie frames to the reconstructions [33]. The resulting dataset of polished particles was used for further 2D and 3D classification using a soft-edge spherical mask to select the best 3D classes. Several runs of 3D classification with different starting seeds and different number of classes were performed to assess reproducibility and consistency. We then applied first a spherical mask to identify the largest difference between the classes, followed by a soft-edged mask together with finer angular sampling and local angular search. At this stage some 3D classes displayed an extra weak density protruding from the side of the matrix arm. Further particle selection on the basis of extensive 3D classification with a finer angular sampling interval of 3.75° using a soft-edge shaped mask, made with the *relion\_mask\_create* module of RELION, and a local angular search range of 5° resulted in two smaller datasets, one containing 29,125 particles showing the well-known complex I shape and one of 9485 particles showing a prominent extra density next to the 49-kDa core subunit (NUCM). Further sorting of the particle images recorded close to focus [19] or with high values of the normalized probability distribution [34] did not improve the maps significantly, probably because these procedures work best at high resolution.

The two datasets were subjected to 3D refinement in RELION and the final maps were post-processed for masking, B-factor determination and map sharpening using the post-processing procedure in RELION [35]. After post-processing the resolution was estimated by the 0.143 FSC criterion as 7.9 Å for complex I and 10.4 Å for the complex I – ST1 assembly. A further refinement of the smaller dataset with local angular search was performed in FREALIGN [36] version 9.11 in mode 1 using the Euler angles, shifts and the soft-edge shaped mask previously obtained with RELION using a global search of 3.75°. This led to an improvement in resolution in the map displaying the extra density from 10.4 to 9.5 Å (Fig. S1).

Before visualization all density maps were corrected for the modulation transfer function (MTF) of the Falcon II direct detector. Maps were sharpened with negative B-factors of 200 Å<sup>2</sup> for complex I and 250 Å<sup>2</sup> for complex I – ST1.

### 2.5. Sequence analysis and homology modelling

A homology model of ST1 was built using the PSIPRED Protein Sequence Analysis Workbench [37] (<http://bioinf.cs.ucl.ac.uk/>) and the HH-Pred toolkit (<http://toolkit.tuebingen.mpg.de/hhpred>) [38] to find the best match between an available structure and the ST1 sequence. From the best matches sorted by sequence identity (>40%) and coverage SseA, an MST of *E. coli*, (1URH) and the rhodanese-like protein

Tum1 from *S. cerevisiae* (3UTN) were selected. These structures were then used as templates to build homology models for ST1 using the server SWISS-MODEL [39] (<http://swissmodel.expasy.org/>).

UCSF Chimera [40] was used to visualize the cryo-EM maps, and rigid body fitting of atomic models was done using the *fit-in-map* module from Chimera.

### 3. Results

Complex I from the aerobic yeast *Y. lipolytica* was solubilized in dodecyl maltoside and purified by His-tag affinity chromatography [23]. Individual complex I particles in vitreous ice on holey carbon film were imaged with a Falcon II direct electron detector in movie mode (see Methods). Reference-free two-dimensional class averages show the characteristic L-shape of complex I. Movie frames were used to correct for beam induced movement and 3D refinement was performed in RELION [31]. Particle polishing [33] was followed by further 2D and 3D classification. A three-dimensional map of *Y. lipolytica* complex I was obtained from 29,125 particles and refined to 7.9 Å resolution (Fig. S1). The overall shape and dimensions of the cryo-EM map agree well with previous structures of *Y. lipolytica* complex I [6,15,41]. Overall, the complex is 250 Å long and 190 Å high with a width of 75 Å for the membrane arm and 115 Å for the matrix arm. The 200 Å membrane arm and 130 Å matrix arm include an angle of ~120°. The eight Fe-S clusters were clearly visible at a resolution above 11 Å (Fig. 1) at the positions of the atomic coordinates in the X-ray structure [15]. The binuclear cluster N1a appears weaker, in agreement with earlier observations that the distal part of the peripheral arm is the most flexible region of the structure [6,11,15]. Most alpha helices in the membrane arm are well resolved, including the characteristic long lateral helix at the C-terminus of the central subunit ND5. The X-ray structure of *Y. lipolytica* complex I [15] fits the cryo-EM map closely (Fig. 2), allowing us to assign all central subunits plus the large accessory subunit NUEM. Prominent density features corresponding to previously assigned accessory subunits, e.g. the functionally important NB4M/ACPM1 domain [42] that protrudes from the peripheral arm, are clearly visible. In addition, we confirm

the position of the C-terminal zinc-binding domain of the recently characterized accessory subunit NUMM [43]. Several of the density features seen in the cryo-EM map were unassigned in the X-ray structure of *Y. lipolytica* complex I. This includes a well-defined density at the tip of the peripheral arm that is in contact with the central 75-kDa subunit. The human complex I accessory subunit NDUFA2 has a typical thioredoxin fold. Its structure was determined by NMR spectroscopy [44]. A homology model of the orthologous NI8M subunit closely matched this prominent unassigned density in the cryo-EM map (Fig. 2).

During 2D classification a weak extra density extending from the peripheral arm became visible in some of the subclasses. Comparison of subclasses with the same orientation of complex I clearly showed that the particle population was heterogeneous (Fig. S2). We concluded that the sample consisted of a mixture of complex I and complex I with an additional protein subunit. Robust 3D classification separated a subclass containing this extra subunit (see Material and Methods section 2.4 for a more detailed description), resulting in a map at 9.5 Å resolution that showed the extra density clearly. The particles contributing to this final map accounted for <20% of the whole dataset (Fig. 3).

Notably, there was no protein corresponding to this extra density in the X-ray structure [6,15]. The complex I from which the crystals had been grown was purified from a strain from which the gene coding for the accessory sulfur transferase subunit ST1 had been deleted, because in the wild-type enzyme this subunit had been found to be present in substoichiometric amounts and was thought to potentially interfere with crystallization [18]. We therefore investigated the possibility that the extra density in our map represents ST1.

The family of sulfur transferases can be divided into two subclasses based on which substrate the enzyme uses, these are thiosulfate:sulfur transferases (TST; E.C. 2.8.1.1) and 3-mercaptopyruvate:sulfur transferases (MST; E.C. 2.8.1.2). In TST the active-site loop displays a CRXGX[R/T] sequence whereas MST contains CG[S/T]GVT [16]. Since the amino acid sequence of *Y. lipolytica* ST1 contains the sequence CGSGVT we conclude that it most likely is an MST (Fig. S3).

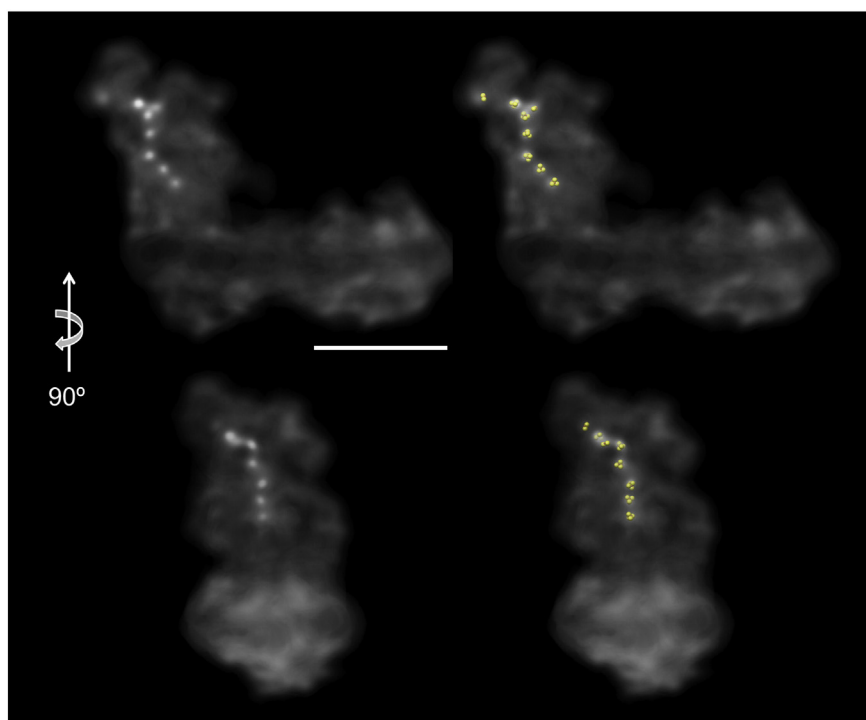


**Fig. 1.** Overview of the cryo-EM map. The complex I map at an intermediate step of refinement (11 Å resolution) shown with UCSF Chimera [40]. Top: side view; bottom: front view. The Fe-S clusters are clearly visible. Right: overlay of the X-ray coordinates of the Fe-S clusters [15]. The scale bar is 100 Å.

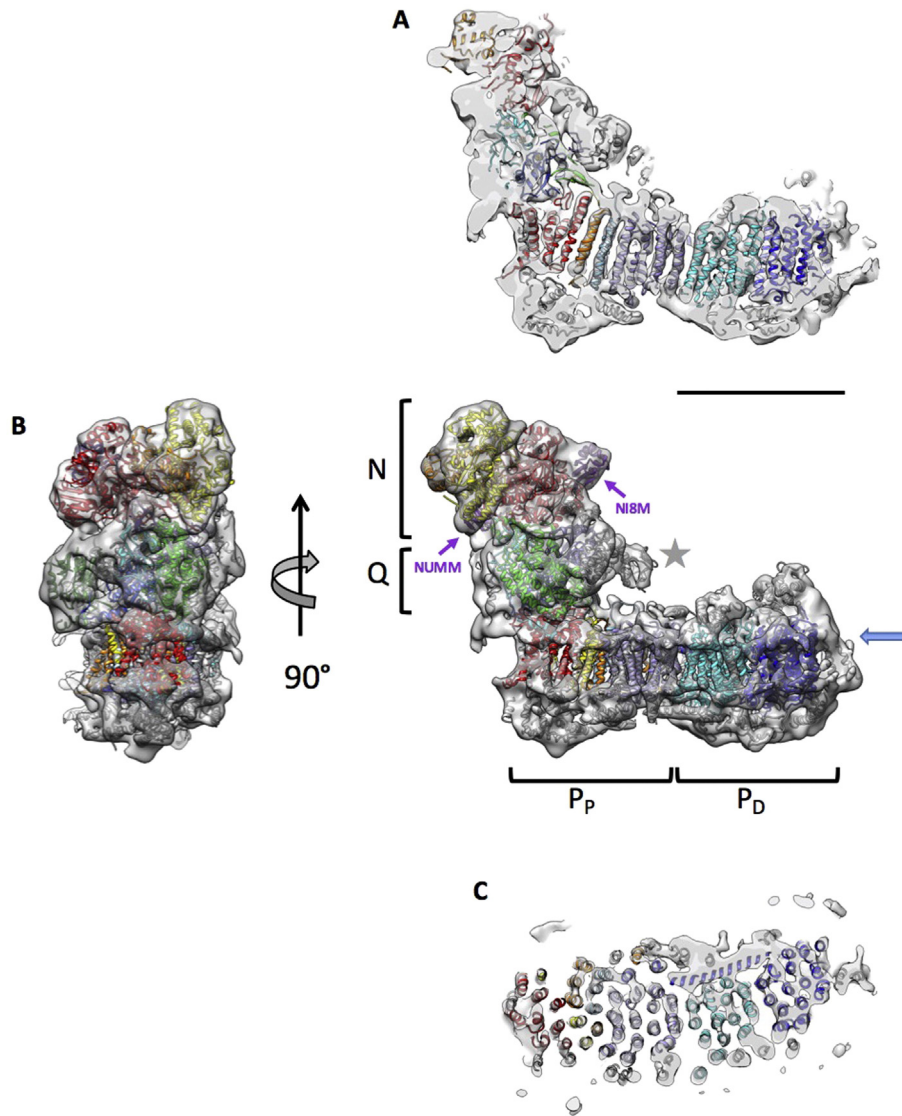


**Fig. 2.** Superposition of the cryo-EM map and X-ray structure of *Y. lipolytica* complex I. **A:** a vertical cross-section through the 7.9 Å cryo-EM map with the fitted X-ray structure (PDB ID: 4WZ7). The peripheral arm comprises the N module extending into the matrix and the Q module docking it onto the membrane arm. The membrane arm contains the P modules and harbors the proton-pumping machinery. Modules and subunits are coloured as in the X-ray structure [15]. N module: red, 75-kDa; yellow, 51-kDa; orange, 24-kDa. Q module: green, 49-kDa; violet, 30-kDa; blue, PSST; cyan, TYKY. P<sub>D</sub> module: dark blue, ND5; cyan, ND4. P<sub>P</sub> module: lilac, ND2; red, ND4L; orange, ND6; yellow, ND3; pink, ND1. Accessory subunit NUEM, forest green. All other accessory subunits and unassigned alpha-helices are shown in grey. **B:** an overview of the EM map from the peripheral arm and rotated by 90°. The accessory subunits N18M and NUMM are both displayed in purple, the grey asterisk highlights the domain that comprises the accessory subunits ACPM1 and NB4M. In **C** a horizontal cross-section through the membrane arm at the height of the blue arrow in **B** shows the fit of the transmembrane alpha helices (TMHs). The scale bar is 100 Å.

To investigate the enzymatic function of ST1 in more detail, we measured MST activity of purified complex I. The generation of H<sub>2</sub>S in the presence of 3-mercaptopyruvate (3-MP) and dithiothreitol (DTT) was monitored by the lead sulfide assay described previously [25,24]. The  $K_m$  value of the sigmoidal kinetics was 47  $\mu\text{M}$  and  $v_{max}$  was 6  $\mu\text{mol min}^{-1} \text{mg}^{-1}$  (Fig. 4A, Table 1). Considering that ST1 corresponds to only 3.5% of the total mass of complex I and taking into account that only 20% of the particles harbor the subunit, this corresponds to an activity of 858  $\mu\text{mol min}^{-1}$  per mg ST1 or a turnover number of  $\sim 480 \text{ s}^{-1}$ . To confirm that this activity was indeed linked to accessory subunit ST1, we expressed the protein in *Escherichia coli* with a C-terminal His<sub>6</sub>-Tag attached and purified it to homogeneity by affinity chromatography and gel filtration (Fig. S4). The observed sigmoidal kinetics gave a  $K_m$  value of 77  $\mu\text{M}$  and a  $v_{max}$  of 290  $\mu\text{mol min}^{-1} \text{mg}^{-1}$  (Fig. 4B, Table 1) corresponding to a turnover number of  $\sim 170 \text{ s}^{-1}$  and indicating a somewhat reduced catalytic efficiency of the heterologously expressed

enzyme. Interestingly, electrons supplied by NADH or NADPH did not lead to any observable MST activity and complex I purified from the ST1 deletion strain [18] did not show any H<sub>2</sub>S formation in presence of 3-MP and DTT. These results clearly demonstrate that the observed sulfur transferase activity of parental complex I can be unequivocally assigned to accessory subunit ST1.

Since the structure of ST1 from *Y. lipolytica* has not been determined we used its amino acid sequence to generate homology models based on the sulfur transferase SseA of *E. coli* (PDB ID:1URH) and the rhodanese-like protein Tum1 from *Saccharomyces cerevisiae* (PDB ID: 3UTN) (Fig. 5). The model based on the 3UTN template was superior, as judged by sequence identity ( $\geq 35\%$ ), sequence coverage after alignment ( $\geq 90\%$ ) and model quality assignment (GMQE value  $\geq 65\%$ ). The model exhibited the typical architecture of two rhodanese-like domains (RLD) and resulted in an excellent fit to the density protruding from the lateral side of the soluble arm (Fig. 5). The N-terminal domain attaches

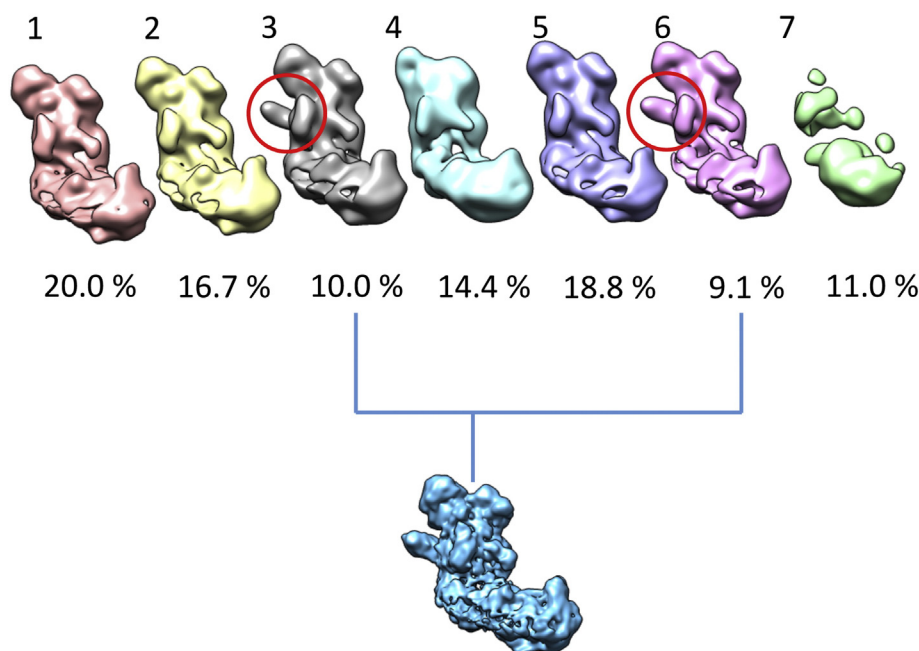


**Fig. 3.** Three-dimensional classification. Overview of the 3D class averages obtained with a soft-edged mask, all displayed at the same density level. The classes are numbered from 1 to 7. The percentage of particles in each class is indicated, corresponding to 8735, 6677, 4471, 6332, 8505, 4980, 5229 for classes 1 to 7 respectively. Two class averages display an extra density on the peripheral arm (red circles); the final refined map combining the particles from these classes is shown in cyan.

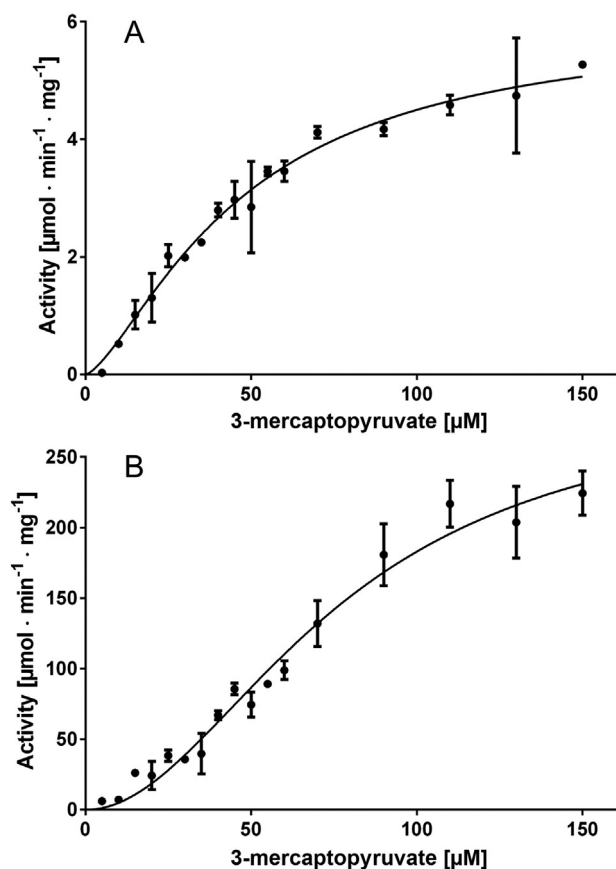


**Fig. 4.** Kinetics of H<sub>2</sub>S generation from 3-mercaptopyruvate by ST1. The generation of H<sub>2</sub>S was monitored by the lead sulfide test [24,25]. **A**, kinetics for complete complex I; **B**, kinetics for isolated ST1 overexpressed in *E. coli*. Note that ST1 accounts for 3.5% of the total mass of complex I and only ~20% of the complex I molecules contain ST1.

to complex I and the catalytic cysteine is located in the distal part of ST1 (Fig. 5). ST1 extends about 50 Å from the soluble arm of complex I, approximately 30 Å above the central plane through the detergent belt surrounding complex I in the 3D map, and thus close to the membrane surface on the matrix side. Fig. 6 shows the refined maps of complex I with or without ST1 with the fitted X-ray structure of *Y. lipolytica* complex I.

#### 4. Discussion

The 7.9 Å resolution cryo-EM map of respiratory complex I from the aerobic yeast *Y. lipolytica* matches the recently published X-ray structure of the same complex closely [15]. The close correlation between the two structures proves that it is the same in detergent solution and 3D crystals and in particular that the X-ray structure is not distorted by crystal packing. Guided by the X-ray structure, assignment of all 14 central subunits and accessory subunit NUEM was straightforward. The 64 transmembrane helices (TMHs) of the core subunits in the membrane arm of the EM map match the X-ray structure exactly. Most of the remaining 18 unassigned helices in the X-ray structure are also visible.

Even though the nominal resolution was lower, the excellent quality of the cryo-EM map made it possible to assign structural elements in regions that were less clear and could not be modeled in the X-ray map. We were able to fit the accessory subunit NI8M in agreement with the assignment of the orthologous subunit in bovine complex I [11] and to confirm the position of accessory subunit NUMM that was recently assigned aided by biochemical and modelling studies [43].

**Table 1**  
MST kinetics.

	$K_m$ ( $\mu\text{M}$ )	$v_{max}$ ( $\mu\text{mol min}^{-1} \text{mg}^{-1}$ )	Hill coefficient
Complex I	$47 \pm 6$	$6.0 \pm 0.5$	1.44
Recombinant ST1	$77 \pm 11$	$290 \pm 30$	1.99

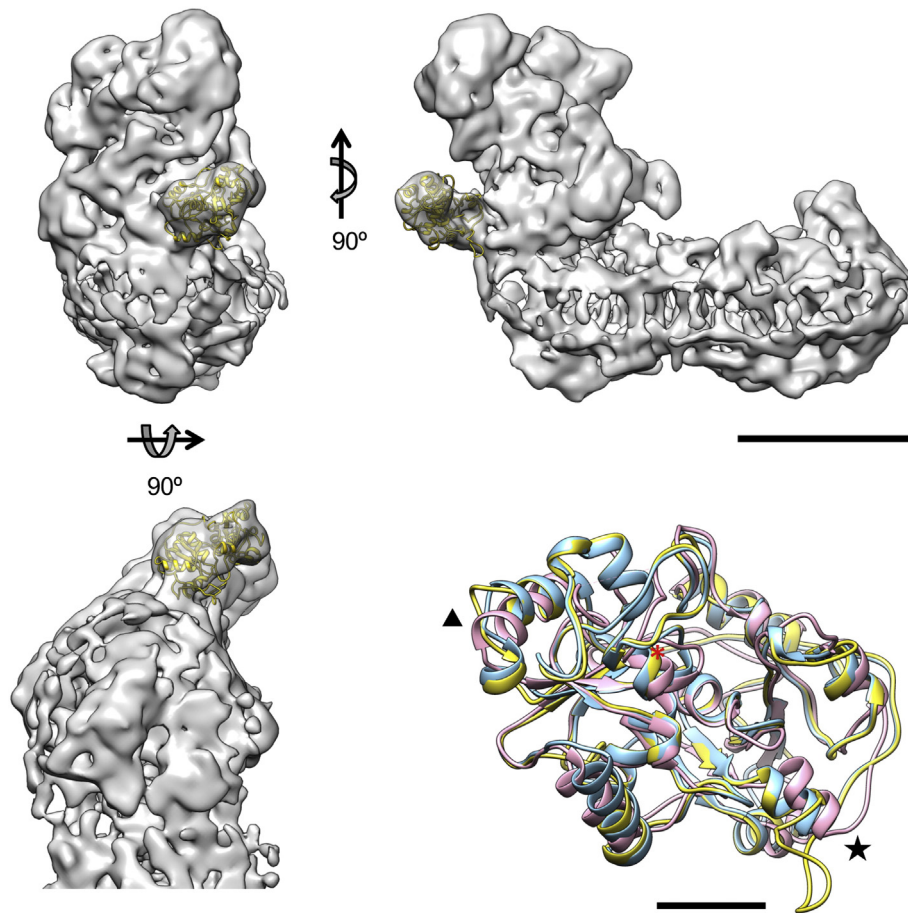


**Fig. 5.** ST1 model fitted into the cryo-EM map. Fit of the ST1 homology model (gold) seen from three different directions (upper and lower left panel). Scale bar: 100 Å. The lower right panel shows an overlay of the homology model of ST1 (gold) with the structures used to generate it, the sulfur transferase SseA of *Escherichia coli* (1URH) in pink and the rhodanese-like protein Tum1 from *Saccharomyces cerevisiae* (3UTN) in light blue. Note that although these proteins differ at the sequence level, the tandem domain three-dimensional characteristic of sulfur transferases is preserved. The N terminus is indicated by a star and the C terminus with a triangle. A red asterisk shows the position of the catalytic cysteine. Scale bar: 15 Å.

The density of the ST1 subunit in the map is similar to that of the other subunits and the local resolution is also the same (Fig. S5), indicating that ST1 is bound in a rigid and specific manner. ST1 is located on the side of the peripheral arm at the height of the central 49-kDa subunit. There is a clear unassigned density at the interface between the 49-kDa and ST1 components that must belong to one of the remaining accessory subunits. It was recently shown that a complex I mutant lacking accessory subunits NUMM and N7BM also lacks subunit ST1 completely [43]. We propose that the three proteins interact and that N7BM in *Y. lipolytica* complex I accounts for the unassigned density at the interface between ST1 and the peripheral arm. This assignment is supported by the recent maps of mammalian complex I where the accessory subunits 13 kDa and B17.2 (orthologues of NUMM and N7BM) reside in this area of the soluble arm [12,13].

Although the well-defined ST1 map density suggests a firm interaction with complex I, ST1 is known to dissociate during BN-PAGE [45]. In line with a previous study [18], our analysis showed that after purification by column chromatography ST1 is clearly substoichiometric, indicating that it can dissociate easily. An association of a sulfur transferase with complex I has so far not been observed, even though biochemical evidence has long suggested a functional link of mitochondrial sulfur metabolism to the respiratory chain [46–49].

Sulfur transferases are ubiquitous enzymes associated with essential physiological processes including cysteine metabolism, cyanide detoxification, thiolation of tRNA and control of cellular redox homeostasis [50–52]. H<sub>2</sub>S released from sulfur transferase is thought to be an important signaling molecule with regulatory functions in higher organisms

[52,53]. Impaired activity of MST in humans causes mercaptolactate-cysteine disulfiduria (MCDU), a rare inheritable disorder that causes behavioral abnormalities such as mental retardation, hypokinetic behavior, and tonic-clonic seizures [54].

Previously it was shown that ST1 has no role in the assembly of complex I, e.g. by providing sulfur for iron-sulfur cluster biogenesis [18]. Here, we showed that ST1 is a functional MST, in line with sequence predictions. The general mechanism proposed for MSTs involves the conversion of 3-mercaptopyruvate originating from cysteine to pyruvate and MST-bound persulfide, which in the presence of a reducing agent is eventually released as H<sub>2</sub>S. The identity of the reducing agent is still unclear, but thiol containing compounds like thioredoxins and glutathione are abundant in the mitochondrial matrix. Thioredoxin or dihydrolipoic acid were suggested to accept and reduce a sulfur atom from an enzyme bound persulfide intermediate in the reaction cycle of human MST [55]. H<sub>2</sub>S was not generated when NADH or NADPH were used as electron donors, excluding a direct link with the redox chemistry of complex I. This observation is in agreement with a separation of the active site cysteine of ST1 in our model and the nearest iron-sulfur cluster by >60 Å, which is too far for efficient electron transfer.

Apart from the beneficial generation of H<sub>2</sub>S as a signaling molecule, the MST reaction might also have negative effects for the cell as H<sub>2</sub>S is known to be toxic and to inhibit cytochrome c oxidase [56,57]. Accumulation of H<sub>2</sub>S to toxic levels could be prevented by directly linking its production in ST1 to a pathway for H<sub>2</sub>S consumption. In mitochondria H<sub>2</sub>S detoxification is executed by sulfide quinone reductase (SQR), a ubiquitous flavoprotein that feeds electrons into the respiratory chain

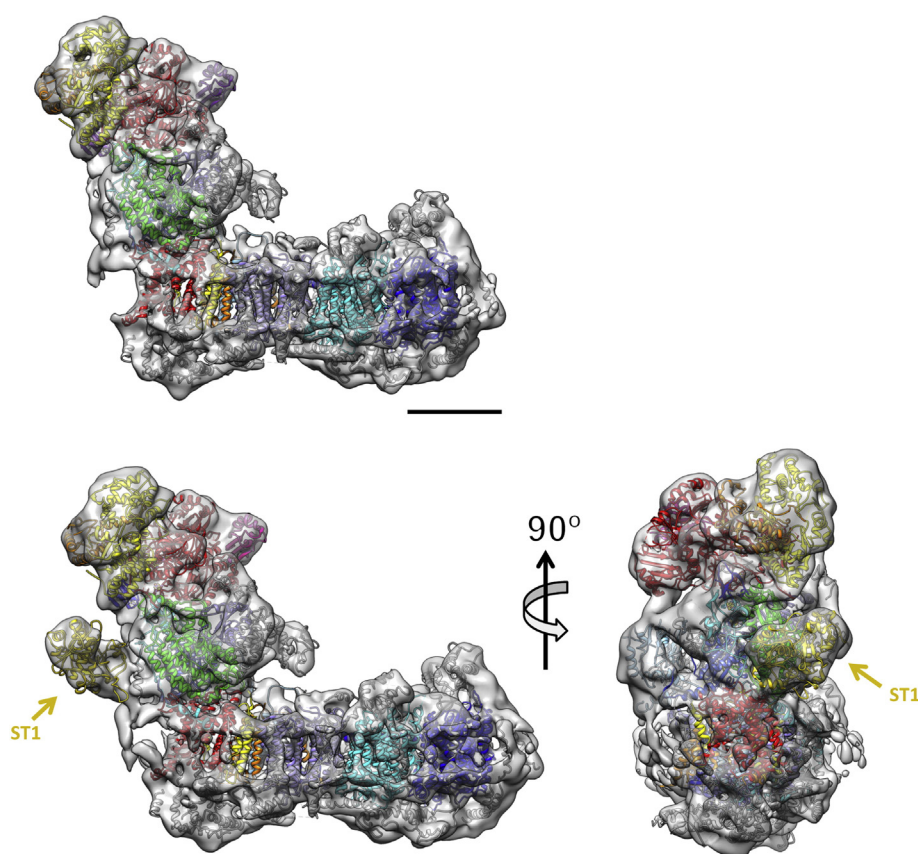


**Fig. 6.** Comparison of cryo-EM maps with and without ST1 density. Complex I without ST1 at 7.9 Å resolution with fitted X-ray structure (upper panel). The low density level matches that of complex I with ST1 at 9.5 Å resolution in the lower panel, with fitted ST1 homology model. The X-ray structure is colored according to [15]. Scale bar: 100 Å.

via ubiquinone [58]. So far, a gene coding for an SQR has not been identified in the *Y. lipolytica* genome, and the similarity between NDH-2 and SQR sequences complicates unequivocal assignments [59]. Our working hypothesis is that an SQR in the mitochondrial membrane of *Y. lipolytica* might interact with ST1 bound to complex I. The dimensions of the gap between ST1 and the membrane would easily accommodate a typical SQR with its predominantly membrane-extrinsic topology [60–62] and such an arrangement would locate SQR close to a source of H<sub>2</sub>S. It is tempting to speculate that complex I provides a structural scaffold that links biogenesis of H<sub>2</sub>S with its instantaneous detoxification and ubiquinone reduction.

Taken together, our data provide structural evidence for a link between sulfur metabolism and respiratory complex I. To our knowledge our findings show for the first time an accessory subunit of respiratory complex I that is enzymatically active. Further work is needed to understand the precise role of ST1 in mitochondrial sulfur metabolism.

#### Accession numbers

The cryo-EM maps were deposited in the wwPDB with accession codes EMD-4110 (complex I consensus map) and EMD-4111 (complex I with ST1).

#### Transparency document

The [Transparency document](#) associated with this article can be found, in the online version.

#### Acknowledgements

We thank Karin Siegmund and Andrea Duchene for excellent technical assistance, Özkan Yildiz and Juan F. Castillo-Hernández for computer

support, Matteo Allegretti for helpful discussions on data collection and image processing, Bruno Marreiros for discussion on hallmarks of SQR/NDH-2 sequences, and Thomas Meier for discussion on ST1-complex I interaction.

This work was supported by the German Research Foundation (ZI 552/4-1 to VZ) and the Excellence Initiative of the German Federal and State Governments (EXC 115).

#### Appendix A. Supplementary data

Supplementary data to this article can be found online at <http://dx.doi.org/10.1016/j.bbabbio.2016.09.014>.

#### References

- [1] J. Hirst, Mitochondrial complex I, *Annu. Rev. Biochem.* 82 (2013) 551–575, <http://dx.doi.org/10.1146/annurev-biochem-070511-103700>.
- [2] U. Brandt, Energy converting NADH:quinone oxidoreductase (complex I), *Annu. Rev. Biochem.* 75 (2006) 69–92, <http://dx.doi.org/10.1146/annurev.biochem.75.103004.142539>.
- [3] E.T. Chouchani, C. Methner, S.M. Nadtochiy, A. Logan, V.R. Pell, S. Ding, A.M. James, H.M. Cocheme, J. Reinhold, K.S. Lilley, L. Partridge, I.M. Fearnley, A.J. Robinson, R.C. Hartley, R.A. Smith, T. Krieg, P.S. Brookes, M.P. Murphy, Cardioprotection by S-nitrosation of a cysteine switch on mitochondrial complex I, *Nat. Med.* 19 (2013) 753–759, <http://dx.doi.org/10.1038/nm.3212>.
- [4] W.J. Koopman, P.H. Willems, J.A. Smeitink, Monogenic mitochondrial disorders, *N. Engl. J. Med.* 366 (2012) 1132–1141, <http://dx.doi.org/10.1056/NEJMra1012478>.
- [5] M.E. Breuer, W.J. Koopman, S. Koene, M. Nooteboom, R.J. Rodenburg, P.H. Willems, J.A. Smeitink, The role of mitochondrial OXPHOS dysfunction in the development of neurologic diseases, *Neurobiol. Dis.* 51 (2013) 27–34, <http://dx.doi.org/10.1016/j.nbd.2012.03.007>.
- [6] C. Hunte, V. Zickermann, U. Brandt, Functional modules and structural basis of conformational coupling in mitochondrial complex I, *Science* 329 (2010) 448–451, <http://dx.doi.org/10.1126/science.1191046>.
- [7] K. Kmita, V. Zickermann, Accessory subunits of mitochondrial complex I, *Biochem. Soc. Trans.* 41 (2013) 1272–1279, <http://dx.doi.org/10.1042/BST20130091>.

- [8] R. Baradaran, J.M. Berrisford, G.S. Minhas, L.A. Sazanov, Crystal structure of the entire respiratory complex I, *Nature* 494 (2013) 443–448, <http://dx.doi.org/10.1038/nature11871>.
- [9] R.G. Efremov, R. Baradaran, L.A. Sazanov, The architecture of respiratory complex I, *Nature* 465 (2010) 441–447.
- [10] R.G. Efremov, L.A. Sazanov, Structure of the membrane domain of respiratory complex I, *Nature* 476 (2011) 414–420, <http://dx.doi.org/10.1038/nature10330>.
- [11] K.R. Vinothkumar, J. Zhu, J. Hirst, Architecture of mammalian respiratory complex I, *Nature* 515 (2014) 80–84, <http://dx.doi.org/10.1038/nature13686>.
- [12] J. Zhu, K.R. Vinothkumar, J. Hirst, Structure of mammalian respiratory complex I, *Nature* 536 (2016) 354–358, <http://dx.doi.org/10.1038/nature19095>.
- [13] K. Fiedorczuk, J.A. Letts, G. Degliesposti, K. Kaszuba, M. Skehel, L.A. Sazanov, Atomic structure of the entire mammalian mitochondrial complex I, *Nature* (2016), <http://dx.doi.org/10.1038/nature19794> (advance online publication).
- [14] J. Zhu, M.S. King, M. Yu, L. Klipcan, A.G. Leslie, J. Hirst, Structure of subcomplex I $\beta$  of mammalian respiratory complex I leads to new supernumerary subunit assignments, *Proc. Natl. Acad. Sci. U. S. A.* 112 (2015) 12087–12092, <http://dx.doi.org/10.1073/pnas.1510577112>.
- [15] V. Zickermann, C. Wirth, H. Nasiri, K. Siegmund, H. Schwalbe, C. Hunte, U. Brandt, Mechanistic insight from the crystal structure of mitochondrial complex I, *Science* 342 (2015) 44–49, <http://dx.doi.org/10.1126/science.1259859>.
- [16] D. Bordo, P. Bork, The rhodanese/Cdc25 phosphatase superfamily. Sequence-structure-function relations, *EMBO Rep.* 3 (2002) 741–746, <http://dx.doi.org/10.1093/embo-reports/kvf150>.
- [17] J.H. Ploegman, G. Drent, K.H. Kalk, W.G.J. Hol, Structure of bovine liver rhodanase. I. Structure determination at 2.5 Å resolution and a comparison of the conformation and sequence of its two domains, *J. Mol. Biol.* 123 (1978) 557–594.
- [18] A. Abdrahmanova, K. Dobrynin, K. Zwicker, S. Kerscher, U. Brandt, Functional sulfurtransferase is associated with mitochondrial complex I from *Yarrowia lipolytica*, but is not required for assembly of its iron-sulfur clusters, *FEBS Lett.* 579 (2005) 6781–6785, <http://dx.doi.org/10.1016/j.febslet.2005.11.008>.
- [19] M. Allegretti, D.J. Mills, G. McMullan, W. Kühlbrandt, J. Vonck, Atomic model of the F<sub>420</sub>-reducing [NiFe] hydrogenase by electron cryo-microscopy using a direct electron detector, *eLife* 3 (2014), e01963, <http://dx.doi.org/10.7554/eLife.01963>.
- [20] M. Liao, E. Cao, D. Julius, Y. Cheng, Structure of the TRPV1 ion channel determined by electron cryo-microscopy, *Nature* 504 (2013) 107–112, <http://dx.doi.org/10.1038/nature12822>.
- [21] I.S. Fernandez, X.C. Bai, T. Hussain, A.C. Kelley, J.R. Lorsch, V. Ramakrishnan, S.H.W. Scheres, Molecular architecture of a eukaryotic translational initiation complex, *Science* 342 (2013) 1240585, <http://dx.doi.org/10.1126/science.1240585>.
- [22] J. Kim, S. Wu, T.M. Tomasiak, C. Mergel, M.B. Winter, S.B. Stiller, Y. Robles-Colmanares, R.M. Stroud, R. Tampe, C.S. Craik, Y. Cheng, Subnanometre-resolution electron cryomicroscopy structure of a heterodimeric ABC exporter, *Nature* 517 (2015) 396–400, <http://dx.doi.org/10.1038/nature13872>.
- [23] N. Kashani-Poor, S. Kerscher, V. Zickermann, U. Brandt, Efficient large scale purification of His-tagged proton translocating NADH:ubiquinone oxidoreductase (complex I) from the strictly aerobic yeast *Yarrowia lipolytica*, *Biochim. Biophys. Acta* 1504 (2001) 363–370.
- [24] P.K. Yadav, K. Yamada, T. Chiku, M. Koutmos, R. Banerjee, Structure and kinetic analysis of H<sub>2</sub>S production by human mercaptopyruvate sulfurtransferase, *J. Biol. Chem.* 288 (2013) 20002–20013, <http://dx.doi.org/10.1074/jbc.M113.466177>.
- [25] T. Chiku, D. Padovani, W. Zhu, S. Singh, V. Vitvitsky, R. Banerjee, H<sub>2</sub>S biogenesis by human cystathionine gamma-lyase leads to the novel sulfur metabolites lantionine and homolantionine and is responsive to the grade of hyperhomocysteinemia, *J. Biol. Chem.* 284 (2009) 11601–11612, <http://dx.doi.org/10.1074/jbc.M808026200>.
- [26] D.J. Mills, S. Vitt, M. Strauss, S. Shima, J. Vonck, De novo modeling of the F<sub>420</sub>-reducing [NiFe]-hydrogenase from a methanogenic archaeon by cryo-electron microscopy, *eLife* 2 (2013), e00218, <http://dx.doi.org/10.7554/eLife.00218>.
- [27] X.-c. Bai, I.S. Fernandez, G. McMullan, S.H.W. Scheres, Ribosome structures to near-atomic resolution from thirty thousand cryo-EM particles, *eLife* 2 (2013), e00461, <http://dx.doi.org/10.7554/eLife.00461>.
- [28] X. Li, P. Mooney, S. Zheng, C.R. Booth, M.-B. Braunfeld, S. Gubbens, D.A. Agard, Y. Cheng, Electron counting and beam-induced motion correction enable near-atomic-resolution single-particle cryo-EM, *Nat. Methods* 10 (2013) 584–590, <http://dx.doi.org/10.1038/nmeth.2472>.
- [29] S.J. Ludtke, P.R. Baldwin, W. Chiu, EMAN: semiautomated software for high-resolution single-particle reconstructions, *J. Struct. Biol.* 128 (1999) 82–97.
- [30] J.A. Mindell, N. Grigorieff, Accurate determination of local defocus and specimen tilt in electron microscopy, *J. Struct. Biol.* 142 (2003) 334–347.
- [31] S.H. Scheres, RELION: implementation of a Bayesian approach to cryo-EM structure determination, *J. Struct. Biol.* 180 (2012) 519–530, <http://dx.doi.org/10.1016/j.jsb.2012.09.006>.
- [32] G. Tang, L. Peng, P.R. Baldwin, D.S. Mann, W. Jiang, I. Rees, S.J. Ludtke, EMAN2: An extensible image processing suite for electron microscopy, *J. Struct. Biol.* 157 (2007) 38–46, <http://dx.doi.org/10.1016/j.jsb.2006.05.009>.
- [33] S.H. Scheres, Beam-induced motion correction for sub-megadalton cryo-EM particles, *eLife* 3 (2014), e03665, <http://dx.doi.org/10.7554/eLife.03665>.
- [34] M.G. Campbell, D. Veasler, A. Cheng, C.S. Potter, B. Carragher, 2.8 Å resolution reconstruction of the Thermoplasma acidophilum 20S proteasome using cryo-electron microscopy, *eLife* 4 (2015), e06380, <http://dx.doi.org/10.7554/eLife.06380>.
- [35] S. Chen, G. McMullan, A.R. Faruqi, G.N. Murshudov, J.M. Short, S.H. Scheres, R. Henderson, High-resolution noise substitution to measure overfitting and validate resolution in 3D structure determination by single particle electron cryomicroscopy, *Ultramicroscopy* 135 (2013) 24–35, <http://dx.doi.org/10.1016/j.ultramic.2013.06.004>.
- [36] N. Grigorieff, FREALIGN: high-resolution refinement of single particle structures, *J. Struct. Biol.* 157 (2007) 117–125, <http://dx.doi.org/10.1016/j.jsb.2006.05.004>.
- [37] D.W. Buchan, F. Minneci, T.C. Nugent, K. Bryson, D.T. Jones, Scalable web services for the PSIPRED Protein Analysis Workbench, *Nucleic Acids Res.* 41 (2013) W349–W357, <http://dx.doi.org/10.1093/nar/gkt381>.
- [38] J. Soding, A. Biegert, A.N. Lupas, The HHpred interactive server for protein homology detection and structure prediction, *Nucleic Acids Res.* 33 (2005) W244–W248, <http://dx.doi.org/10.1093/nar/gki408>.
- [39] M. Biasini, S. Bienert, A. Waterhouse, K. Arnold, G. Studer, T. Schmidt, F. Kiefer, T.G. Cassarino, M. Bertoni, L. Bordoli, T. Schwede, SWISS-MODEL: modelling protein tertiary and quaternary structure using evolutionary information, *Nucleic Acids Res.* 42 (2014) W252–W258, <http://dx.doi.org/10.1093/nar/gku340>.
- [40] E.F. Pettersen, T.D. Goddard, C.C. Huang, G.S. Couch, D.M. Greenblatt, E.C. Meng, T.E. Ferrin, UCSF Chimera: a visualisation system for exploratory research and analysis, *J. Comput. Chem.* 25 (2004) 1605–1612, <http://dx.doi.org/10.1002/jcc.20084>.
- [41] M. Radermacher, T. Ruiz, T. Clason, S. Benjamin, U. Brandt, V. Zickermann, The three-dimensional structure of complex I from *Yarrowia lipolytica*: a highly dynamic protein, *J. Struct. Biol.* 154 (2006) 269–279.
- [42] H. Angerer, M. Radermacher, M. Mańkowska, M. Steger, K. Zwicker, H. Heide, I. Wittig, U. Brandt, V. Zickermann, The LYR protein subunit NB4M/NDUFA6 of mitochondrial complex I anchors an acyl carrier protein and is essential for catalytic activity, *Proc. Natl. Acad. Sci. U.S.A.* 111 (2014) 5207–5212, <http://dx.doi.org/10.1073/pnas.1322438111>.
- [43] K. Kmita, C. Wirth, J. Warnau, S. Guerrero-Castillo, C. Hunte, G. Hummer, V.R. Kaila, K. Zwicker, U. Brandt, V. Zickermann, Accessory NUMM (NDUF56) subunit harbors a Zn-binding site and is essential for biogenesis of mitochondrial complex I, *Proc. Natl. Acad. Sci. U. S. A.* 112 (2015) 5685–5690, <http://dx.doi.org/10.1073/pnas.1424353112>.
- [44] C. Brockmann, A. Diehl, K. Rehbein, H. Strauss, P. Schmieder, B. Korn, R. Kühne, H. Oschkinat, The oxidized subunit B8 from human complex I adopts a thioredoxin fold, *Structure* 12 (2004) 1645–1654, <http://dx.doi.org/10.1016/j.str.2004.06.021>.
- [45] N. Morgner, V. Zickermann, S. Kerscher, I. Wittig, A. Abdrahmanova, H.D. Barth, B. Brutschy, U. Brandt, Subunit mass fingerprinting of mitochondrial complex I, *Biochim. Biophys. Acta* 1777 (2008) 1384–1391, <http://dx.doi.org/10.1016/j.bbabi.2008.08.001>.
- [46] M.K. Grieshaber, S. Volkel, Animal adaptations for tolerance and exploitation of poisonous sulfide, *Annu. Rev. Physiol.* 60 (1998) 33–53, <http://dx.doi.org/10.1146/annurev.physiol.60.1.33>.
- [47] T.M. Hildebrandt, M.K. Grieshaber, Redox regulation of mitochondrial sulfide oxidation in the lugworm, *Arenicola marina*, *J. Exp. Biol.* 211 (2008) 2617–2623, <http://dx.doi.org/10.1242/jeb.019729>.
- [48] K. Modis, C. Coletta, K. Erdelyi, A. Papapetropoulos, C. Szabo, Intramitochondrial hydrogen sulfide production by 3-mercaptopyruvate sulfurtransferase maintains mitochondrial electron flow and supports cellular bioenergetics, *FASEB J.* 27 (2013) 601–611, <http://dx.doi.org/10.1096/fj.12-216507>.
- [49] F. Bouillaud, F. Blachier, Mitochondria and sulfide: a very old story of poisoning, feeding, and signaling? *Antioxid. Redox Signal.* 15 (2011) 379–391, <http://dx.doi.org/10.1089/ars.2010.3678>.
- [50] B. Sorbo, Sulfite and complex-bound cyanide as sulfur acceptors for rhodanese, *Acta Chem. Scand.* 11 (1957) 628–633.
- [51] P.M. Palenchar, C.J. Buck, H. Cheng, T.J. Larson, E.G. Mueller, Evidence that ThiI, an enzyme shared between thiamin and 4-thiouridine biosynthesis, may be a sulfurtransferase that proceeds through a persulfide intermediate, *J. Biol. Chem.* 275 (2000) 8283–8286.
- [52] O. Kabil, R. Banerjee, Enzymology of H<sub>2</sub>S biogenesis, decay and signaling, *Antioxid. Redox Signal.* 20 (2014) 770–782, <http://dx.doi.org/10.1089/ars.2013.5339>.
- [53] R. Wang, Two's company, three's a crowd: can H<sub>2</sub>S be the third endogenous gaseous transmitter? *FASEB J.* 16 (2002) 1792–1798, <http://dx.doi.org/10.1096/fj.02-0211hyp>.
- [54] N. Nagahara, M. Nagano, T. Ito, K. Shimamura, T. Akimoto, H. Suzuki, Antioxidant enzyme, 3-mercaptopyruvate sulfurtransferase-knockout mice exhibit increased anxiety-like behaviors: a model for human mercaptolactate-cysteine disulfiduria, *Sci. Rep.* 3 (2013) 1986, <http://dx.doi.org/10.1038/srep01986>.
- [55] Y. Mikami, N. Shibuya, Y. Kimura, N. Nagahara, Y. Ogasawara, H. Kimura, Thioredoxin and dihydroliipoic acid are required for 3-mercaptopyruvate sulfurtransferase to produce hydrogen sulfide, *Biochem. J.* 439 (2011) 479–485, <http://dx.doi.org/10.1042/BJ20110841>.
- [56] L.C. Petersen, The effect of inhibitors on the oxygen kinetics of cytochrome c oxidase, *Biochim. Biophys. Acta* 460 (1977) 299–307.
- [57] B.C. Hill, T.C. Woon, P. Nicholls, J. Peterson, C. Greenwood, A.J. Thomson, Interactions of sulphide and other ligands with cytochrome c oxidase. An electron-paramagnetic-resonance study, *Biochem. J.* 224 (1984) 591–600.
- [58] R. Yong, D.G. Searcy, Sulfide oxidation coupled to ATP synthesis in chicken liver mitochondria, *Comp. Biochem. Physiol. B Biochem. Mol. Biol.* 129 (2001) 129–137.
- [59] B.C. Marreiros, F.V. Sena, F.M. Sousa, A.P. Batista, M.M. Pereira, Type II NADH:quinone oxidoreductase family: phylogenetic distribution, structural diversity and evolutionary divergences, *Environ. Microbiol.* (2016), <http://dx.doi.org/10.1111/1462-2920.13352> (in press).
- [60] M. Marcia, U. Ermler, G. Peng, H. Michel, The structure of *Aquifex aeolicus* sulfide:quinone oxidoreductase, a basis to understand sulfide detoxification and respiration, *Proc. Natl. Acad. Sci. U. S. A.* 106 (2009) 9625–9630, <http://dx.doi.org/10.1073/pnas.0904165106>.
- [61] J.A. Brito, F.L. Sousa, M. Stelter, T.M. Bandejas, C. Vonnheim, M. Teixeira, M.M. Pereira, M. Archer, Structural and functional insights into sulfide:quinone oxidoreductase, *Biochemistry* 48 (2009) 5613–5622, <http://dx.doi.org/10.1021/bi9003827>.
- [62] M. Marcia, U. Ermler, G. Peng, H. Michel, A new structure-based classification of sulfide:quinone oxidoreductases, *Proteins* 78 (2010) 1073–1083, <http://dx.doi.org/10.1002/prot.22665>.